remote sensing

MDPI

Article

Spectral Cross-Calibration of VIIRS Enhanced Vegetation Index with MODIS: A Case Study Using Year-Long Global Data

Kenta Obata [1,2,*], Tomoaki Miura [2], Hiroki Yoshioka [3], Alfredo R. Huete [4] and Marco Vargas [5]

Received: 6 November 2015; Accepted: 29 December 2015; Published: 5 January 2016
Academic Editors: Changyong Cao, Dongdong Wang and Prasad S. Thenkabail

1 National Institute of Advanced Industrial Science and Technology (AIST), Geological Survey of Japan, the Research Institute of Geology and Geoinformation, Central 7, 1-1-1 Higashi, Tsukuba, Ibaraki 305-8567, Japan
2 Department of Natural Resources and Environmental Management, University of Hawaii at Manoa, 1910 East West Road, Sherman 101, Honolulu, HI 96822, USA; tomoakim@hawaii.edu
3 Department of Information Science and Technology, Aichi Prefectural University, 1522-3 Ibara, Nagakute, Aichi 480-1198, Japan; yoshioka@ist.aichi-pu.ac.jp
4 The Plant Functional Biology and Climate Change Cluster, University of Technology Sydney, P.O. Box 123, Broadway NSW 2007, Australia; Alfredo.Huete@uts.edu.au
5 Center for Satellite Applications and Research, National Oceanic and Atmospheric Administration, College Park, MD 20740, USA; marco.vargas@noaa.gov
* Correspondence: kenta.obata@aist.go.jp; Tel.: +81-29-861-3623

Abstract: In this study, the Visible Infrared Imaging Radiometer Suite (VIIRS) Enhanced Vegetation Index (EVI) was spectrally cross-calibrated with the Moderate Resolution Imaging Spectroradiometer (MODIS) EVI using a year-long, global VIIRS-MODIS dataset at the climate modeling grid (CMG) resolution of 0.05°-by-0.05°. Our cross-calibration approach was to utilize a MODIS-compatible VIIRS EVI equation derived in a previous study [Obata *et al.*, *J. Appl. Remote Sens.*, vol.7, 2013] and optimize the coefficients contained in this EVI equation for global conditions. The calibrated/optimized MODIS-compatible VIIRS EVI was evaluated using another global VIIRS-MODIS CMG dataset of which acquisition dates did not overlap with those used in the calibration. The calibrated VIIRS EVI showed much higher compatibility with the MODIS EVI than the original VIIRS EVI, where the mean error (MODIS minus VIIRS) and the root mean square error decreased from −0.021 to −0.003 EVI units and from 0.029 to 0.020 EVI units, respectively. Error reductions on the calibrated VIIRS EVI were observed across nearly all view zenith and relative azimuth angle ranges, EVI dynamic range, and land cover types. The performance of the MODIS-compatible VIIRS EVI calibration appeared limited for high EVI values (*i.e.*, EVI > 0.5) due likely to the maturity of the VIIRS dataset used in calibration/optimization. The cross-calibration methodology introduced in this study is expected to be useful for other spectral indices such as the normalized difference vegetation index and two-band EVI.

Keywords: EVI; VIIRS; MODIS; spectral compatibility; cross-calibration; CMG data

1. Introduction

Biophysical parameters retrieved from Earth observation data are crucial for improving our understanding of biosphere–atmosphere interactions (e.g., [1]). Spectral vegetation indices (VIs) derived from remotely sensed data have been used successfully to estimate biophysical parameters, for example, the fraction of photosynthetically active radiation (FAPAR), leaf area index (LAI) [2], and green vegetation fraction [3]. The normalized difference vegetation index (NDVI) has been the

most widely used index. The NDVI has been found to be highly correlated with the biophysical properties of vegetation canopies and able to reduce the effects of topographic shading and shadowing for seasonal trend analyses of terrestrial vegetation [4] and global carbon cycle modeling [5]. However, the NDVI is affected by other factors such as soil background brightness and aerosol contamination [6]. The enhanced vegetation index (EVI), developed for Moderate Resolution Imaging Spectroradiometer (MODIS) of the National Aeronautics and Space Administration's (NASA) Earth Observing System (EOS), was designed to optimize the vegetation signal with improved sensitivity in high biomass regions and improved vegetation monitoring through a decoupling of the canopy background signal and a reduction in atmospheric aerosol influences that affect the NDVI [7]:

$$\mathrm{EVI} = G\frac{\rho_n - \rho_r}{\rho_n + C_1\rho_r - C_2\rho_b + L} \quad (1)$$

where ρ are the total- or partial (uncorrected for aerosols)-atmosphere corrected reflectances, subscripts "n", "r", and "b" represent the near-infrared (NIR), red, and blue bands, respectively, L is the canopy background brightness adjustment factor, and C_1 and C_2 are the coefficients of the aerosol resistance term. The coefficients adopted in the MODIS EVI algorithm are: L = 1.0, C_1 = 6.0, C_2 = 7.5, and G (gain factor) = 2.5 [8]. MODIS was designed to be highly calibrated and to have explicit atmospheric corrections and, thereby, EVI has been used in a wide range of applications including ecosystem resilience studies [9], an estimation of gross primary production (GPP) [10], and evapotranspiration estimates [11].

The Visible Infrared Imaging Radiometer Suite (VIIRS) sensor onboard Suomi-National Polar-orbiting Partnership (S-NPP) has begun to collect data, which is slated to replace the Advanced Very-High Resolution Radiometer (AVHRR) onboard the National Oceanic and Atmospheric Administration (NOAA) polar-orbiting satellite series with afternoon overpass, and to continue the MODIS highly calibrated data stream. The VIIRS geophysical product, termed environmental data records (EDRs), includes the top-of-atmosphere (TOA) NDVI and top-of-canopy (TOC) EVI [12]. VI continuity/compatibility across AVHRR, MODIS, and VIIRS is of great importance for understanding spatial and temporal dynamics of global vegetation over several decades.

Differences in sensor and platform characteristics, and product generation algorithms, however, cause systematic errors in VI time series across sensors. Spectral bandpasses are one major issue in using multi-sensor data [13] and, thus, this study was focused on inter-sensor spectral compatibility and calibration of the EVI between MODIS and VIIRS. Numerical experiments using Earth Observing-1 (EO-1) Hyperion data showed that VIIRS EVI was higher than MODIS EVI with the maximum differences reaching 0.040 EVI units over a tropical forest-savanna eco-gradient in Brazil [14] and the same trend was observed in a Hyperion-based bandpass simulation analysis conducted over AERONET sites in the conterminous United States [15]. An initial assessment of actual VIIRS EVI data was reported in [16]; an average (bias) of VIIRS EVI minus MODIS EVI (a gain factor G = 2.5) was zero when EVI was zero, but always positive for the rest of EVI dynamic range, indicating that VIIRS EVI was always higher than the MODIS counterpart. Another EVI compatibility analysis using Aqua MODIS (L2G daily 500 m, Collection 5) and VIIRS (L2G daily 500 m) showed that an average of MODIS EVI minus VIIRS EVI was −0.022 for North America for August 2013 [17], indicating that VIIRS EVI was generally higher than MODIS EVI. The positive errors in VIIRS EVI over MODIS EVI were consistently observed in both Hyperion-simulated and actual sensor data. It should be noted that the errors might contain not only the spectral effects but the effects of other factors including differences in the product generation algorithm such as atmospheric correction and quality flags, geolocation errors, spatial resolution differences, and radiometric calibration uncertainties, to name a few.

Numerous cross-sensor VI translation equations, especially for the NDVI, have been proposed and the techniques can basically be applied to the EVI. These techniques for cross-sensor VI translations can be categorized into three approaches as summarized in [17]: (1) polynomial based approach [18–23];

(2) band-averaging approach [24–26]; and (3) vegetation isoline-based approach [27,28]. In our previous study, the vegetation isoline-based approach, that translates a reflectance of an arbitrary wavelength to that of another wavelength in the solar-reflective region based on the radiative transfer theory [29], was employed and a MODIS-compatible EVI with VIIRS spectral bandpasses was derived [17]. The derived equation had four coefficients that were a function of soil, canopy, and atmosphere, e.g., soil line slope, leaf area index (LAI), and aerosol optical thickness (AOT). The MODIS-compatible EVI resulted in a reasonable level of accuracy when the coefficients were fixed at values found via optimization for model-simulated and actual sensor data (the North American continent in August 2013), demonstrating the potential practical utility of the derived equation [17].

The primary objective of this study was to calibrate the MODIS-compatible VIIRS EVI equation for global conditions. "Optimized" coefficients were sought using a year-long, global VIIRS-MODIS dataset at the climate modeling grid (CMG) resolution of 0.05°-by-0.05°. A secondary objective of this study was to develop a cross-calibration protocol that can be used to revise the optimum coefficients when a new dataset becomes available. We evaluated the extent to which errors decreased by applying the obtained VIIRS EVI equation with the optimized coefficients on global data and the degree to which errors varied as a function of sun-target-sensor viewing geometry, EVI values, and land cover type.

2. MODIS-Compatible VIIRS EVI

The MODIS-compatible VIIRS EVI was derived using the vegetation isoline equations [17]. The equations analytically approximate and describe the vegetation isoline, which is defined as the line formed between the reflectances at two different wavelengths for an optically and structurally constant canopy and a constant atmospheric condition over varying canopy background brightness [29]. A horizontally infinite homogeneous atmospheric layer was assumed and a portion of the target area was assumed to be covered with a homogeneous canopy. It was further assumed that the radiative transfer problem in both the covered and uncovered areas could be simulated independently by modeling a horizontally homogeneous canopy and Lambertian soil surface, respectively. The first-order photon interactions between soil and canopy and between canopy and atmosphere were considered (higher order interaction terms were truncated) for deriving the vegetation isoline equations.

In deriving the MODIS-compatible VIIRS EVI, we first obtained equations that related the VIIRS blue, red, and NIR (M3, I1, and I2 bands) to the MODIS respective counterparts (band 3, band 1, and band 2) [17] using the vegetation isoline equations

$$\rho_{b,m} = A_b \rho_{b,v} + D_b \tag{2a}$$

$$\rho_{r,m} = A_r \rho_{r,v} + D_r \tag{2b}$$

$$\rho_{n,m} = A_n \rho_{n,v} + D_n \tag{2c}$$

where $\rho_{b,m}$, $\rho_{r,m}$, and $\rho_{\mathrm{n,m}}$ are MODIS blue, red, and NIR band reflectances which are TOC or partial (uncorrected for aerosol)-atmosphere corrected reflectances that are modeled by adding aerosol layer over the canopy; $\rho_{b,v}$, $\rho_{r,v}$, and $\rho_{n,v}$ are VIIRS counterparts. A_b, A_r, and A_n (slopes of the isoline equation for blue, red, and NIR bands) and D_b, D_r, and D_n (offsets of the isoline equation for blue, red, and NIR bands) are dependent on the reflectance and transmittance of the canopy and atmospheric layers, and the soil line slope and offset for MODIS blue and VIIRS blue, MODIS red and VIIRS red, and MODIS NIR and VIIRS NIR band pairs, respectively.

We then substituted Equations (2a–c) for the MODIS reflectances in Equation (1) to express the MODIS EVI equation as a function of VIIRS reflectances [17],

$$\hat{v}_m = G \frac{\rho_{v,n} - K_1 \rho_{v,r} + K_2}{\rho_{v,n} + K_1 C_1 \rho_{v,r} - K_3 C_2 \rho_{v,b} + K_4} \tag{3}$$

and

$$K_1 = \frac{A_r}{A_n} \tag{4a}$$

$$K_2 = \frac{D_n - D_r}{A_n} \tag{4b}$$

$$K_3 = \frac{A_b}{A_n} \tag{4c}$$

$$K_4 = \frac{C_1 D_r + D_n - C_2 D_b + L}{A_n} \tag{4d}$$

where $\hat{v}_m$ is the MODIS-compatible VIIRS EVI. The coefficients in Equation (3), K_1, K_2, K_3, and K_4 vary with the soil, vegetation, and aerosol conditions [17] and that the exact translation is possible only when the exact conditions of soil, vegetation, and atmosphere are known.

3. Calibration of MODIS-Compatible VIIRS EVI Using Global Data

3.1. Cross-Calibration (Optimization) Algorithm

Our approach for calibrating MODIS-compatible VIIRS EVI was to obtain a single set of K_i (i = 1, 2, 3, 4) that minimizes differences between the MODIS-compatible VIIRS EVI ($\hat{v}_m$) and the MODIS EVI (v_m) via non-linear regression. As in our previous study [17], the mean absolute difference (MAD) between $\hat{v}_m$ and v_m was used as the merit function for the non-linear regression:

$$\min_{K_i \in \mathbb{R}} MAD\left(K_1, K_2, K_3, K_4\right) \tag{5}$$

and

$$MAD\left(K_1, K_2, K_3, K_4\right) = \frac{1}{N} \sum_{i=1}^{N} \left| v_{m,i} - \hat{v}_{m,i}\left(K_1, K_2, K_3, K_4\right) \right| \tag{6}$$

This merit function could include multiple local minima and thereby the optimum, best solution was determined by searching for the global minimum using the Nelder-Mead simplex method in Optimization Toolbox of MATLAB® R2015a (MathWorks Inc., Natick, MA, USA). The algorithm was run without derivatives, but with 100 initial guesses. In the reminder, the best set of coefficients obtained by the algorithm are denoted by K_i^* (i = 1, 2, 3, 4).

3.2. Data Extraction

Aqua MODIS (Collection 5) and S-NPP VIIRS (Archive Set (AS) 3001) global daily 0.05-degree (climate modeling grid, CMG) resolution surface reflectance data were obtained for a one-year period of 1 August 2012 through 31 July 2013 for the calibration/optimization exercise. This VIIRS surface reflectance dataset (AS 3001) was produced at the NASA Science Investigator-led Processing System (SIPS), formerly known as the VIIRS Land Product Evaluation and Analysis Tool Element (Land PEATE), using the Joint Polar Satellite System (JPSS) near-real-time Interface Data Processing Segment (IDPS) software. The products of AS 3001 from SIPS should match the corresponding product from IDPS [30]. The VIIRS CMG surface reflectance algorithm was based on the MODIS Collection 5 CMG surface reflectance product generation algorithm [31]. The MODIS and VIIRS data were screened for cloud, cloud shadow, high aerosol loading, and snow/ice using quality assessment (QA) information and land quality flags (QF), respectively.

The spectral data employed in the calibration/optimization consisted of pairs of MODIS and VIIRS reflectances that were obtained on the same dates at the same CMG locations for the same specific angle bins. Seven view zenith angle bins were defined as $\theta_j \leqslant \theta_v < \theta_j + 8.0$ where θ_v is the view zenith angle in degrees and θ_j's for j = 1, 2, $\cdots$, 7 were 0.0, 8.0, 16.0, 24.0, 32.0, 40.0, 48.0, respectively. The two relative azimuth angle (θ_a) bins in degree were defined, corresponding to the backward scattering ($-90.0 < \theta_a < 90.0$) and forward scattering ($-180.0 < \theta_a -< 90.0$, $90.0 < \theta_a < 180.0$)

directions. The mean and standard deviation (STD) of solar zenith angle differences between MODIS and VIIRS (MODIS minus VIIRS) were −1.2 and 1.8, respectively, and differences between relative azimuth angles were 1.9 and 5.7, respectively.

More than 6 million pairs were found in and extracted from the one-year data. The calibration/optimization exercise of the MODIS-compatible VIIRS EVI would have been too computationally intensive if all the pairs had been used. Thus, the minimum necessary number of sample pairs was determined by a numerical experiment in which the number of sample pairs for the optimization was increased from 10^2 to 10^6 with a logarithmic increment in the sample size. MAD between MODIS-compatible EVI and MODIS EVI, represented by p_n (n = 1, 2, ⋯, 30), was computed for the n-th dataset. Differences between adjacent MADs (d_n), or between p_n and p_{n+1}, were computed to provide information regarding the rate of change in MAD for n = 1, 2, ⋯, 29,

$$d_n = p_{n+1} - p_n \tag{7}$$

A random sample of the size of 10^2 reflectance pairs were selected from the extracted pairs in the above step, from which p_1 was computed. An additional number of randomly selected reflectance pairs were added to the first random sample to create a sample for p_2 from which first p_2 and then d_1 were computed. Likewise, d_n were computed until n = 29. This procedure was repeated 10 times to provide 10 sets of d_n. To evaluate variability in d_n, d_n was plotted as a function of the sample size (Figure 1). d_n changed by $\pm$0.0003 when the sample size was equal to or greater than 41,754 highlighted by the vertical dashed line in Figure 1. This converges to zero when the number of samples is further increased. The threshold of 0.0003 was qualitatively determined after computing d_n, but the change in MAD was small enough or nearly independent of the sample size when it was equal to or greater than 41,754. The minimum necessary number of samples in this study, therefore, was assumed to be equal to or greater than 41,754.

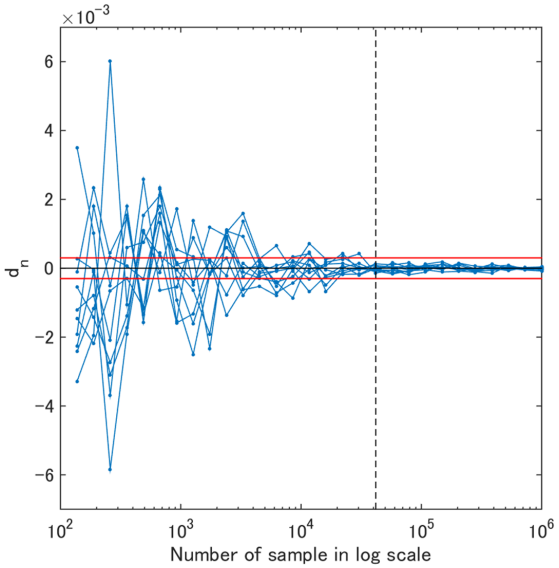

Figure 1. Variability in rate of change in the mean absolute difference (MAD) between MODIS-compatible EVI and MODIS EVI (d_n) as a function of the number of sample data. A vertical dashed line corresponds to the number of sample 41,754.

Prior to data extraction for the optimization, we eliminated anomalies in the sample data. Spectral data pairs were rejected if EVIs were lower than −0.05 or greater than 1.0. This is because, some VIIRS EVI exceeded the upper value of the valid range of MODIS EVI used in MOD13 series [32], *i.e.*, 1.0, due probably to cloud leakage and/or residual snow/ice contamination. In addition, when VIIRS M3 surface reflectance exceeded 0.3 (possible cloud leakage or residual snow/ice contamination),

the pair was removed. If $\delta_1 <$ median $(\delta_1) - \sigma$ or $\delta_1 >$ median $(\delta_1) + \sigma$ (δ_1 is MODIS EVI minus VIIRS EVI (see Equation (8)); σ is 0.09, the STD of δ_1), the pair was removed as an outlier. The value of σ, 0.09 was considered large enough since the maximum difference between MODIS and VIIRS EVI calculated from model-simulated (noise free) data was less than 0.02 for nadir view [17] and less than 0.03 for off-nadir (60 degrees) view (results not shown here). The possible causes of these outliers as identified are discussed in next subsection.

In this study, sample data were selected in order for the EVI frequencies to be as uniform as possible. Also, the data were selected to be more uniform with respect to sun-target-sensor viewing geometry. First, 200,000 pairs of MODIS and VIIRS spectra, which satisfied the conditions for the data extraction described above, were randomly selected and extracted from each of the 14 angular bins (seven variations in view zenith angle and two variations in relative azimuth angle), and then 2,800,000 pairs of data were created by combining the 14 data sets. The sample data were then selected randomly from the 2,800,000 pairs but to be uniform with respect to the EVI value. The relative frequency of EVI of the 2,800,000 data is shown by the blue line in Figure 2 whereas the frequency of sample data that were used in the optimization is shown by the red line in Figure 2. The total number of reflectance pairs was 137,278, which is greater than the minimum necessary number of sample (41,754) and computationally-acceptable for the optimization.

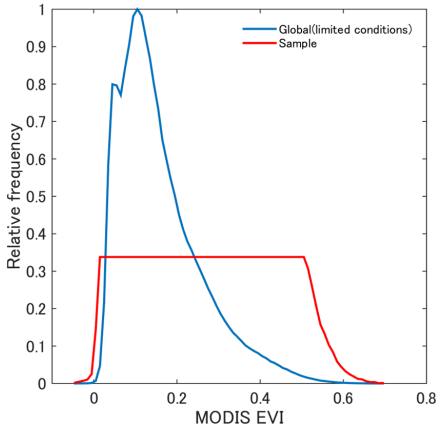

Figure 2. Relative frequency of MODIS EVI extracted from the climate modeling grid (CMG) data with the limited conditions regarding view zenith and azimuth angles and time period, denoted by blue line and that of data used for optimization (sample data), denoted by red line.

The percentage of the pair of reflectances in respective angular ranges is shown in Table 1. Since the angular distribution in each EVI bin (e.g., 0.01 in EVI unit) would not be identical, the resultant values of the percentages were not uniform. The number of samples for backward scattering tended to increase with increasing view angle. On the contrary, it decreased as view angle increased in the forward scattering direction when the view angle was larger than 32.0.

Table 1. Percentage for the number of pairs of MODIS and VIIRS reflectance spectra in each angular condition.

		Relative Azimuth Angle	
		$-90.0 < \theta_a < 90.0$ (Backward Scattering)	**$-180.0 < \theta_a < -90.0$, $90 < \theta_a < 180$ (Forward Scattering)**
View zenith angle	$0.0 < \theta_v < 8.0$	6.7	6.3
	$8.0 < \theta_v < 16.0$	6.9	6.3
	$16.0 < \theta_v < 24.0$	7.7	6.5
	$24.0 < \theta_v < 32.0$	9.3	6.4
	$32.0 < \theta_v < 40.0$	10.4	5.1
	$40.0 < \theta_v < 48.0$	9.6	4.3
	$48.0 < \theta_v < 56.0$	10.7	3.8

3.3. Optimization Results

The errors between MODIS EVI and VIIRS EVI are written as δ_1, and errors between MODIS EVI and MODIS-compatible EVI with the optimized coefficients (K_i^*, i = 1, 2, 3, 4) are written as δ_2^*,

$$\delta_1 = v_m - v_v \tag{8}$$

$$\delta_2^* = v_m - \hat{v}_m^* \left(K_1^*, K_2^*, K_3^*, K_4^*\right) \tag{9}$$

where v_m, v_v, and $\hat{v}_m^*$ are MODIS EVI, VIIRS EVI, and MODIS-compatible VIIRS EVI with the optimized set of coefficients.

In Figure 3a, MODIS EVI minus VIIRS EVI (δ_1) are plotted as a function of MODIS EVI. On average, δ_1 was the smallest at EVI = 0, decreased until approximately EVI = 0.2, and remained nearly the same for higher EVI values (Figure 3a). The mean, STD, and root mean square error (RMSE) of δ_1 were -0.019, 0.028, and 0.034, respectively (Table 2). The mean values of MODIS minus VIIRS reflectances were -0.009, -0.003, and -0.011 for the blue, red, and NIR bands, respectively. In general, higher VIIRS blue and NIR reflectances contributed to higher VIIRS EVI values than the MODIS counterparts. The effect of spectral bandpasses and additional uncertainties caused by radiometric calibration could add systematic errors to surface reflectances. While δ_1 had less scattering about the trend at lower (0 to 0.2) EVI values, large positive values in δ_1 were observed with increasing EVI values (Figure 3a). This indicates that VIIRS EVI shows relatively smaller values than MODIS EVI, which can likely be attributed to cloud leakage in VIIRS Cloud Mask (VCM). Other sources of systematic and random errors arise from differences in the maturity of the atmospheric correction algorithms, including aerosol optical properties, relative geolocation errors between the sensors, and influences associated with differences in spatial compositing for generating CMG data. Although the input reflectance pairs were carefully selected to have the same sun-target-view geometric conditions, subtle differences in the geometric conditions remained in many pairs, being an additional source of random/systematic errors that are inevitable for this cross-sensor comparison.

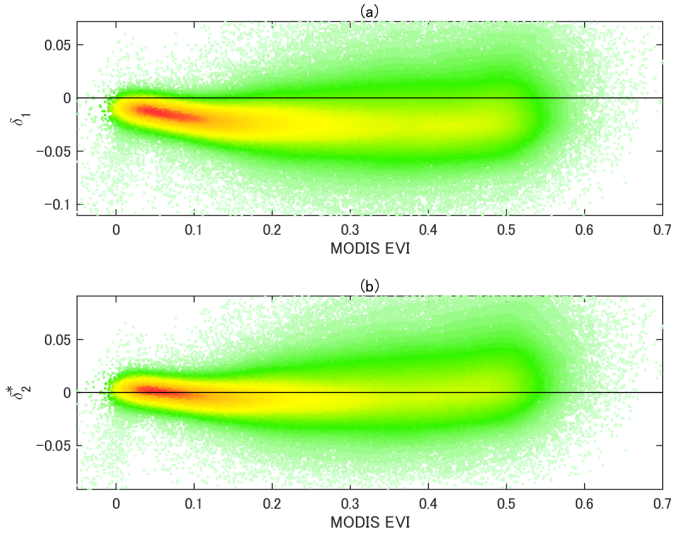

Figure 3. Density plots of EVI differences using the data for the calibration. (**a**) Density plot of MODIS EVI minus VIIRS EVI (δ_1) *vs.* MODIS EVI; (**b**) Density plot of MODIS EVI minus MODIS-compatible VIIRS EVI (δ_2^*) *vs.* MODIS EVI.

Table 2. Statistics of MODIS EVI minus VIIRS EVI (δ_1) and MODIS EVI minus MODIS-compatible VIIRS EVI obtained in the optimization (δ_2^*).

	Mean	STD	RMSE
δ_1	−0.019	0.028	0.034
δ_2^*	0.002	0.028	0.028

The optimization was performed using the extracted data and resultant coefficients are summarized in Table 3. K_1^* and K_4^* were close to unity and K_2^* was close to zero, whereas K_3^* were 0.874. The validity of these values can be evaluated based on the slope and offset calculated from the linear regression between MODIS and VIIRS reflectances. The slope and offset of the linear regression between the VIIRS blue reflectance (x-axis) and MODIS counterpart (y-axis) were 0.813 and 0.0032, respectively, and similarly, 0.934 and 0.0039 for the VIIRS red reflectance and MODIS counterpart, and 0.915 and 0.013 for the VIIRS NIR reflectance and MODIS counterpart. We consider the slopes of the regressions as the averages of the slope of the vegetation isoline equations in Equations (2a–c) for the MODIS-VIIRS CMG data, $\overline{A}_b$, $\overline{A}_r$, and $\overline{A}_n$ (= 0.813, 0.915, and 0.939) and consider the offsets of the regressions as the average values of offsets of the isoline equations, $\overline{D}_b$, $\overline{D}_r$, and $\overline{D}_n$ (= 0.0032, 0.0039, and 0.013). The averages of K_i ($\overline{K}_i$) using these averages can be computed as: $\overline{K}_1 = \overline{A}_r/\overline{A}_n = 1.026$, $\overline{K}_2 = \left(\overline{D}_n - \overline{D}_r\right)/\overline{A}_n = 0.010$, $\overline{K}_3 = \overline{A}_b/\overline{A}_n = 0.888$, and $\overline{K}_4 = (C_1\overline{D}_r + \overline{D}_n - C_2\overline{D}_b + L)/\overline{A}_n = 1.107$. These values are very similar to K_i^*; especially they are the same for K_1. Therefore, the optimized, best coefficients K_i^* can be reasonable.

Table 3. Values of optimized coefficients obtained using the sample data.

K_1^*	K_2^*	K_3^*	K_4^*
1.026	−0.001	0.874	1.022

Thus, the calibrated MODIS-compatible EVI ($\hat{v}_m^*$) is written as

$$\hat{v}_m^* = G\frac{\rho_{v,n} - K_1^*\rho_{v,r} + K_2^*}{\rho_{v,n} + K_1^*C_1\rho_{v,r} - K_3^*C_2\rho_{v,b} + K_4^*} \quad (10)$$

Figure 3b shows MODIS-compatible VIIRS EVI minus MODIS EVI (δ_2^*) and that the MODIS-compatible VIIRS EVI with optimized coefficients resulted in a lower error magnitude than VIIRS EVI, *i.e.*, a reduction of the mean difference from 0.019 (δ_1) to 0.002 (δ_2^*). The STD of δ_2^* (0.028) was the same as that of δ_1 (0.028) because the errors were included in both sensors, especially in VIIRS. The RMSE of δ_2^* (0.028) was lower than that of δ_1 (0.034) because of the reduction in the systematic differences.

Figure 4a,b show the spatial distributions of δ_1 and δ_2^*, respectively. In plotting δ_1 and δ_2^* in map format, when multiple error values were found for a single grid, their average value is plotted for the grid. Errors were not measured over all of the grids because the MODIS and VIIRS sun-target-view geometry matchup were found over limited geographic areas. Note that the size of the colored dots is larger than the actual grid size (0.05°-by-0.05°) for improved visualization. Fewer samples seen in tropical forests and high northern latitude regions were due to frequent cloud cover and snow/ice cover. Generally, large negative values in δ_1 were found everywhere, especially in the southeast area of the South American continent, India, West Europe, the western and southern part of Africa, and the northern part of the Eurasian continent. Positive errors were found in the regions that also showed large negative errors and where vegetation are found. Such samples might have been impacted by factors other than spectral bandpasses as mentioned before. Positive errors were also observed in the regions showing lower magnitudes of negative and positive values in δ_1 (−0.03~0.01) such as

sparsely/less vegetated areas and desert including Australia, northern Africa, the central part of Asia, and the southern part of South American continent.

Figure 4b shows the spatial distribution of δ_2^*. The negative values in δ_1 were corrected over the globe by the MODIS-compatible EVI. Areas that showed negative errors in Figure 4a resulted in smaller magnitude of errors. However, positive errors were not properly corrected and remained or increased in their magnitude, in particular, over the southeast of South America and Europe. Clusters of negative errors (approximately −0.01) were observed in Africa, Australia, east South America, and the northern Eurasian continent (the areas heavily impacted by either persistent cloud cover or winter snow cover).

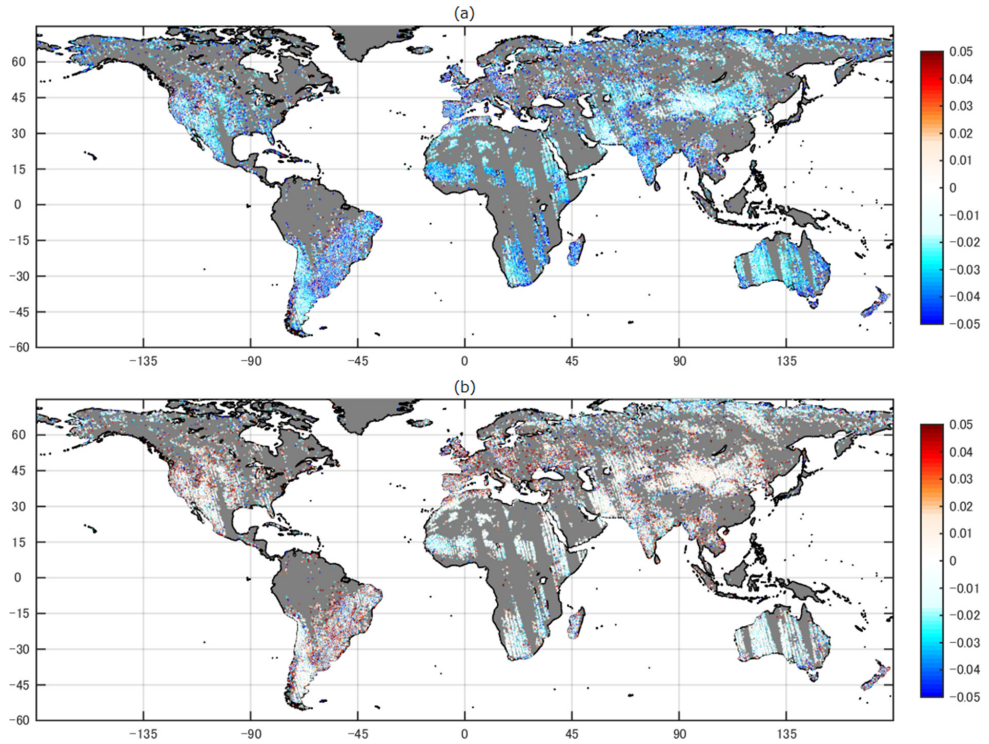

Figure 4. (**a**) Spatial distribution of MODIS EVI minus VIIRS EVI (δ_1) over geographic coordinate for the calibration; (**b**) Spatial distribution of MODIS EVI minus MODIS-compatible EVI (δ_2^*).

4. Evaluation of MODIS-Compatible VIIRS EVI

The MODIS-compatible VIIRS EVI with the optimized coefficients (in Table 3) was evaluated using another dataset, *i.e.*, MODIS and VIIRS global, daily CMG data of which acquisition dates did not overlap with those used in the calibration/optimization. The period of data for the evaluation spanned between 8/1/2013 and 11/30/2013 (four months). The total number of MODIS and VIIRS reflectance pairs, which fell in any of the angular bins described in Section 3.2, was more than 2.8 million from which an evaluation dataset was randomly extracted. The size of this subsample was 200,000. This evaluation dataset had different frequencies over angular and EVI bins from the one used in the previous section.

A density plot of MODIS EVI minus VIIRS EVI (δ_1) as a function of MODIS EVI is shown in Figure 5a. Trends of negative biases and high density in lower EVI values were similar to Figure 3a but the appearance of the plot (distribution of dots) was different because of different scenarios in extracting sample data. The mean of the error (−0.021) was similar to that obtained from the calibration dataset in Figure 3a (−0.019), whereas STD and RMSE (0.021 and 0.029) of this evaluation dataset were smaller than those in Figure 3a (0.028 and 0.034) as summarized in Table 4. Figure 5b shows a density plot of MODIS EVI minus MODIS-compatible EVI (δ_2^*) as a function of MODIS EVI. The absolute average of δ_2^* (0.003) was reduced from that of δ_1 (0.021). STD of δ_2^* (0.020) was slightly lower than

that of δ_1 (0.021). RMSE of δ_2^* (0.020) was reduced from that of δ_1 (0.029). These results indicate that the coefficients obtained in the previous section were reasonable.

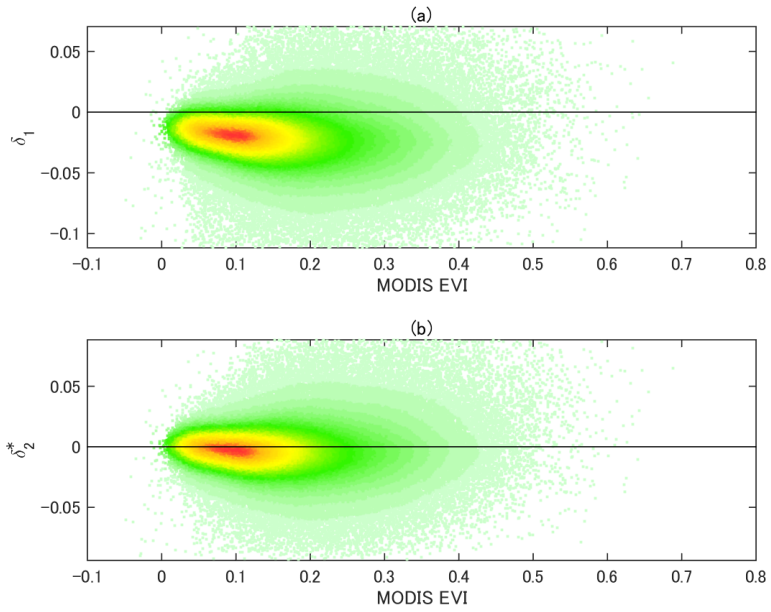

Figure 5. Density plots of EVI differences using the data for the evaluation. (**a**) Density plot of MODIS EVI minus VIIRS EVI (δ_1) *vs.* MODIS EVI; (**b**) Density plot of MODIS EVI minus MODIS-compatible VIIRS EVI (δ_2^*) *vs.* MODIS EVI.

Table 4. Statistics of MODIS EVI minus VIIRS EVI (δ_1) and MODIS EVI minus MODIS-compatible VIIRS EVI (δ_2^*) for the evaluation.

	Mean	STD	RMSE
δ_1	−0.021	0.021	0.029
δ_2^*	−0.003	0.020	0.020

Figure 6a,b show the spatial distribution of MODIS EVI minus VIIRS EVI (δ_1) and MODIS EVI minus MODIS-compatible EVI (δ_2^*), respectively, for evaluation data. Spatial trends of errors in Figure 6 are very similar to those in Figure 4. The spatial coverage of Figure 6 is slightly wider than Figure 4 since the sample size of the evaluation dataset (200,000) was larger than that of the calibration/optimization dataset (137,278). The number of positive error occurrences in Figure 6b appears slightly smaller than that in Figure 4b because of the two different scenarios used in obtaining the evaluation and calibration datasets. For example, the southern part of the South American continent shows fewer dots of positive errors (red dots) compared to Figure 4b.

The MODIS-compatible VIIRS EVI was further evaluated by examining its performance with respect to sun-target-sensor viewing angle, EVI dynamic range, and land cover type. Mean, STD, and RMSE of δ_2^* and δ_1 were computed and those of δ_2^* were divided by the respective counterparts of δ_1, referred to as the ratio of mean (RM), ratio of STD (RS), and ratio of RMSE (RR), for each angle bin, each EVI bin, and each land cover type (Figures 7–9 respectively). The MODIS Land Cover Type Yearly CMG (MCD12C1 [33], resolution of 0.05°-by-0.05°) for 2012 was used to identify the land cover type of each CMG pixel (the 17-class International Geosphere-Biosphere Programme (IGBP) classification) [34].

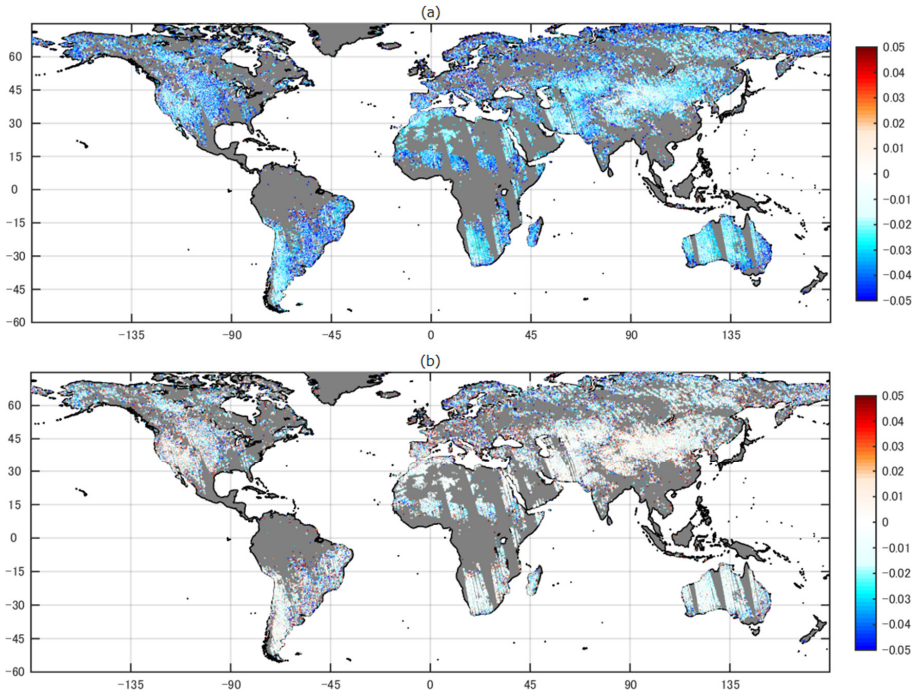

Figure 6. (**a**) Spatial distribution of MODIS EVI minus VIIRS EVI (δ_1) over geographic coordinate for the evaluation; (**b**) Spatial distribution of MODIS EVI minus MODIS-compatible EVI (δ_2^*).

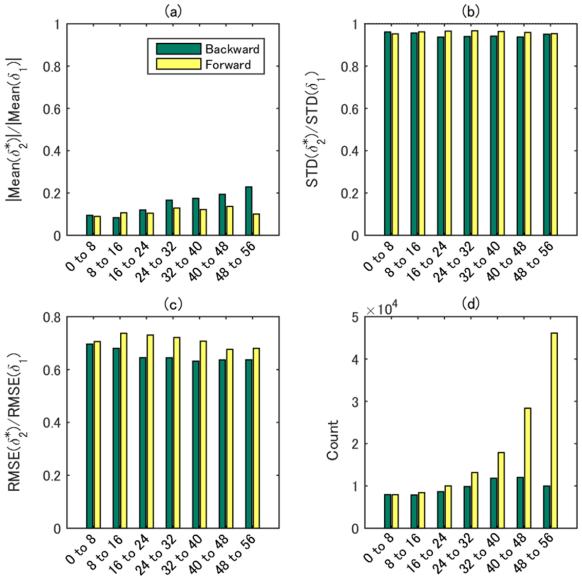

Figure 7. (**a**) Ratio of absolute mean of difference between MODIS EVI minus MODIS-compatible VIIRS EVI (δ_2^*) to that between MODIS EVI minus VIIRS EVI (δ_1) for angular-dependent data (characterized by backward or forward scatterings and view zenith angle); (**b**) Ratio of STD for δ_2^* to that for δ_1; (**c**) Ratio of RMSE for δ_2^* to that for δ_1; (**d**) Frequency of angular distribution in data for evaluation.

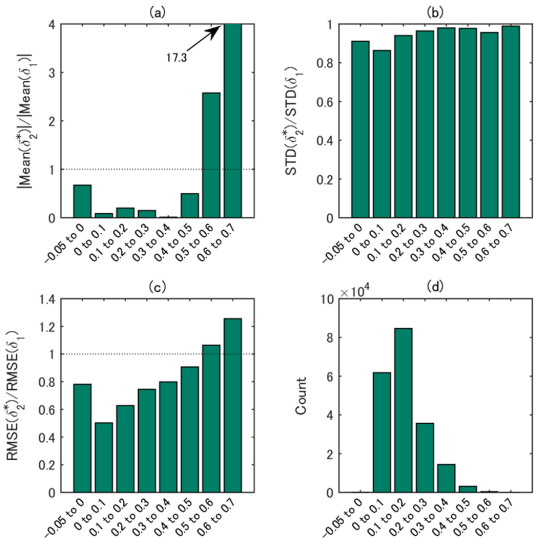

Figure 8. (**a**) Ratio of absolute mean of difference between MODIS EVI minus MODIS-compatible VIIRS EVI (δ_2^*) to that between MODIS EVI minus VIIRS EVI (δ_1) for EVI-dependent data; (**b**) Ratio of STD for δ_2^* to that for δ_1; (**c**) Ratio of RMSE for δ_2^* to that for δ_1; (**d**) Frequency of EVI distribution in data for evaluation.

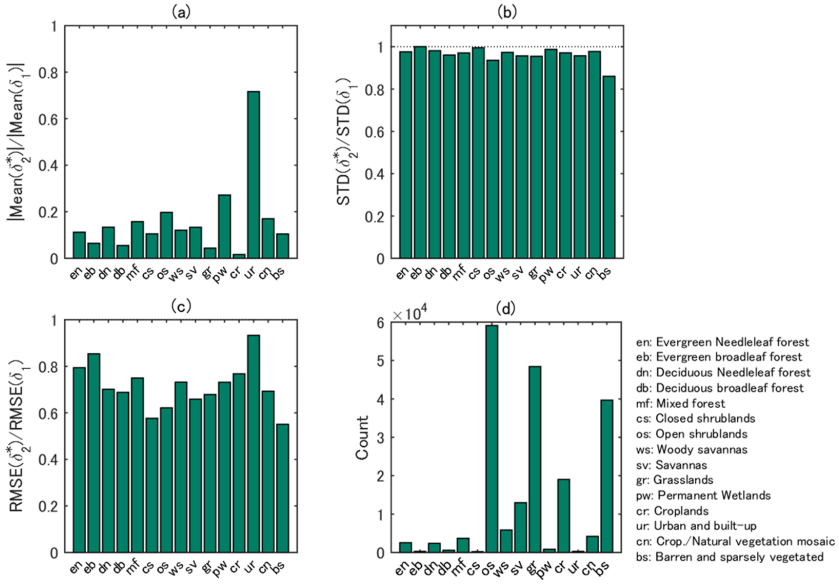

Figure 9. (**a**) Ratio of absolute mean of difference between MODIS EVI minus MODIS-compatible VIIRS EVI (δ_2^*) to that between MODIS EVI minus VIIRS EVI (δ_1) for land cover-dependent data; (**b**) Ratio of STD for δ_2^* to that for δ_1; (**c**) Ratio of RMSE for δ_2^* to that for δ_1; (**d**) Frequency of land cover type distribution in data for evaluation.

The RM increased with view zenith angle for the backward scattering geometry, while it remained nearly the same over the view zenith angle range examined here for the forward scattering direction (Figure 7a). The RS was close to one for both the backward and forward scattering directions, but was slightly smaller for the former than the latter (Figure 7b). The RR was less than 0.8 and smaller for the backward scattering (Figure 7c). It tended to decrease with increasing view angles. The MODIS-compatible EVI performed better for the forward scattering direction in terms of bias but better for the backward scattering direction from the perspective of variability. Figure 7d shows the frequency distribution of each angular condition for this evaluation dataset. The frequency of

backward scattering does not show a strong angular dependency, whereas that of forward scattering showed a monotonic increasing trend.

Dependencies of the improvement of RM, RS, and RR on EVI values from MODIS are shown in Figure 8. Note that the maximum MODIS EVI in our evaluation was 0.688. The RM differed largely across EVI bins (Figure 8a). The bias was the smallest for the EVI range of 0.3–0.4 and was the largest for higher EVI values (from 0.5 to 0.7). Whereas the RS was less than unity and varied a little across EVI bins (Figure 8b), the RR varied greatly from 0.5 to 1.25 (Figure 8c). According to the histogram of this dataset (Figure 8d), most of samples were in the EVI range between 0 and 0.5. Since the coefficients of the MODIS-compatible VIIRS EVI are sensitive to canopy greenness [17], a smaller number of samples in higher EVI values would have been a source of the large RM and RR for that EVI value range. It should be noted that cloud leakage in VCM could degrade the performance of the atmospheric correction algorithm, which may likely be associated with densely vegetated areas due to persistent cloud coverage.

Land cover dependencies of RM, RS, and RR are shown in Figure 9a–c, respectively. Note that data corresponding to "Water" and "Permanent snow and ice" were excluded from this evaluation. The RM was less than 0.4 except for the urban and built-up (ur) cover type (Figure 9a). The RS was close to unity (Figure 9b). The RR was smaller than unity, and showed large improvements for barren and sparsely vegetated area (bs), closed shrublands (cs), and open shrublands (os) followed by savanna (sv) and grass land (gr) (Figure 9c). The urban and built-up area, in general, shows totally different spectral characteristics from vegetated areas, which might have caused the largest RM and RR. Figure 9d shows the land cover frequency of this evaluation dataset. The sample sizes of os, gr, and bs were large, and a general negative correlation between the sample size and the improvements in statistics was observed. The forest cover types where high EVI values are expected (first five cover types in Figure 9a–d) showed some improvements in the statistics, although samples with large EVI values resulted in larger errors. The MODIS/VIIRS EVI tended to fall approximately between 0.1 and 0.5 (0.25 in average) for forest types, in which the MODIS-compatible VIIRS EVI showed higher performance than in the higher EVI value range.

5. Discussions

The coefficients obtained through the calibration/optimization using the one-year global dataset were (K_1^*, K_2^*, K_3^*, K_4^*) = (1.026, −0.001, 0.874, 1.022). The optimum coefficients obtained for North America in August 2013 in our previous study [17], represented here by K'_i (i = 1, 2, 3, 4), were (K'_1, K'_2, K'_3, K'_4) = (0.947, 0.010, 0.265, 0.995). These differences in the optimum coefficient values resulted from the spatiotemporal coverages of the calibration datasets used in the present and previous studies. It should be noted that K_i^* obtained in this study fell in or approached the range of coefficients simulated by radiative transfer models (PROSAIL and 6S code) [17]. The maximum and minimum of K_i (i = 1, 2, 3, 4) obtained in the model simulation were (0.980, 1.024), (−0.002, 0.004), (0.695, 0.935), (0.879, 1.020), respectively. K_2^* (−0.001) and K_3^* (0.874) fell within their corresponding ranges, and K_1^* (1.026) and K_4^* (1.022) slightly greater than the ranges. Since the simulation of coefficients was performed by varying optical thickness of vegetation canopy and aerosol layer but by fixing angular condition, considerations of angular variations in the present study could widen the ranges of coefficients characterized by the maximum and minimum to include $K^*{}_i$ obtained in this study. Further investigation is required to fully understand the relationship between the optimum $K^*{}_i$ values from actual sensor data and ranges of coefficients simulated using radiative transfer models.

The derived equation of MODIS-compatible VIIRS EVI was a non-linear function of K_i, and therefore the optimization of K_i corresponds to the non-linear regression. The small non-linear biases, however, still remained in the δ_2^* (MODIS EVI minus MODIS-compatible VIIRS EVI) in Figure 3b. The comparison of our algorithm with alternative models such as polynomials is certainly important and worthy to evaluate, which is a focus of future work.

The calibrated MODIS-compatible VIIRS EVI showed less compatibility with MODIS EVI over higher EVI values (>0.5). MODIS-VIIRS reflectance pairs that had large positive values in δ_2^* (MODIS EVI minus MODIS-compatible EVI) also had positive values in δ_1 (MODIS EVI minus VIIRSE EVI). However, a Hyperion-based bandpass simulation analysis conducted over AERONET sites only found negative values in MODIS EVI minus VIIRS EVI [15]. This discrepancy implies that these large positive δ_1 values were likely caused by other potential factors than the bandpass differences, such as cloud leakage in VCM which decreases VIIRS EVI and increases δ_1 and δ_2^*, and the maturity status (quality level) of the input surface reflectance data.

The VIIRS surface reflectance product was on a "beta" maturity status for the data period used in this study. Likewise, the VIIRS sensor data record (SDR), the input to the VIIRS surface reflectance product, reached a provisional status in March 2013 [31]. Quality issues associated with the VIIRS surface reflectance data that we noticed included cloud leakage [17,35], aerosol optical thickness [36,37], and VIIRS algorithmic differences from MODIS. The leakage of small clouds resulted in large biases in the surface reflectance intermediate product (IP) which were not documented in QFs [16]. Therefore, spatial averaging for generating CMG pixels could have operated differently between MODIS and VIIRS due primarily to the cloud leakage in VCM. The MODIS/VIIRS pixels involved in area-averaging for generating CMG pixels heavily depend on algorithmic accuracy for cloud detection over the cloudy area. Such dependency caused the situation that the number of pixels, *i.e.*, the areas used to compute CMG reflectances, was not identical between sensors even if the area for the averaging (0.05°-by-0.05°) was the same location. This could subsequently impose substantial differences between CMG reflectances of sensors, in addition to cloud contamination. Significant improvements have, however, been made to these input products since the commencement of this study and additional improvements are planned (e.g., [38,39]). The same and additional analyses using the VIIRS surface reflectance product with a higher maturity status (e.g., provisional or validated stage-1) should allow to examine and identify the factor(s) that caused this apparent poor calibration results for high EVI values and to obtain more refined calibration results of the equation/coefficients.

Coefficients in the MODIS-compatible EVI to be optimized are also influenced by characteristics in sample data and an optimization algorithm. The sample data are characterized by several factors including maturity (accuracy) of the product, the number of samples, frequencies in sun-target-viewing geometry, observation time period, and land cover types. The optimization of coefficients depends on the merit function and the algorithm to search for the optimum solution. The algorithm comprised by the merit function of MAD and the search algorithm of the Nelder-Mead simplex method starting from multiple initial guesses performed properly for the problem of the EVI optimization, which involves multiple local minima.

6. Conclusions

The MODIS-compatible VIIRS EVI was obtained via cross-calibration using a year-long global dataset (MODIS and VIIRS CMG) and was subsequently evaluated with an additional dataset not used for the calibration/optimization. The dataset for obtaining the optimum set of coefficients was selected in order for EVI (and angular) frequencies to be as uniform as possible across all view zenith angles, relative azimuthal angles, and EVI values. The evaluation results showed a significant decrease in the difference between the VIIRS EVI and MODIS EVI upon cross-calibration, the mean error (absolute value) and RMSE having decreased from 0.021 to 0.003 EVI units, and from 0.029 to 0.020 EVI units, respectively. The random and systematic errors in VIIRS data due to the VIIRS product generation algorithms are expected to decrease, which should further improve the performance of the MODIS-compatible VIIRS EVI upon re-calibration with a new, higher maturity level dataset.

The cross-calibration methodology introduced in this study should be useful not only for the EVI cross-calibration, but also for cross-calibrating other vegetation indices, such as the NDVI and two-band EVI (EVI2) [40] and, thus, has the potential to contribute to addressing continuity of spectral vegetation indices across optical sensors for long term global vegetation monitoring.

Acknowledgments: This work was supported by a NOAA JPSS contract (T.M.) and was partially supported by a JSPS KAKENHI Grant Number 15H02856 (H.Y.).

Author Contributions: Kenta Obata and Tomoaki Miura designed the concept of this study, developed the calibration protocol, and wrote the manuscript; Kenta Obata performed the numerical experiment; Hiroki Yoshioka and Alfredo Huete participated in the discussions on the interpretation of results and contributed to editing and revision of the manuscript; Marco Vargas assisted in the interpretation and discussion of results with his knowledge on the VIIRS algorithm and product characteristics.

Conflicts of Interest: The authors declare no conflict of interest.

References

1. Los, S.O. Analysis of trends in fused AVHRR and MODIS NDVI data for 1982–2006: Indication for a CO_2 fertilization effect in global vegetation. *Glob. Biogeochem. Cycles* **2013**, *27*, 318–330. [CrossRef]
2. Nemani, R.R.; Keeling, C.D.; Hashimoto, H.; Jolly, W.M.; Piper, S.C.; Tucker, C.J.; Myneni, R.B.; Running, S.W. Climate-driven increases in global terrestrial net primary production from 1982 to 1999. *Science* **2003**, *300*, 1560–1563. [CrossRef] [PubMed]
3. Jiang, L.; Kogan, F.N.; Guo, W.; Tarpley, J.D.; Mitchell, K.E.; Ek, M.B.; Tian, Y.; Zheng, W.; Zou, C.-Z.; Ramsay, B.H. Real-time weekly global green vegetation fraction derived from advanced very high resolution radiometer-based NOAA operational global vegetation index (GVI) system. *J. Geophys. Res. Atmos.* **2010**, *115*. [CrossRef]
4. Eastman, J.; Sangermano, F.; Machado, E.; Rogan, J.; Anyamba, A. Global Trends in Seasonality of Normalized Difference Vegetation Index (NDVI), 1982–2011. *Remote Sens.* **2013**, *5*, 4799–4818. [CrossRef]
5. Hall, F.; Masek, J.G.; Collatz, G.J. Evaluation of ISLSCP Initiative II FASIR and GIMMS NDVI products and implications for carbon cycle science. *J. Geophys. Res.* **2006**, *111*, D22S08. [CrossRef]
6. Matsushita, B.; Yang, W.; Chen, J.; Onda, Y.; Qiu, G. Sensitivity of the Enhanced Vegetation Index (EVI) and Normalized Difference Vegetation Index (NDVI) to Topographic Effects: A Case Study in High-density Cypress Forest. *Sensors* **2007**, *7*, 2636–2651. [CrossRef]
7. Huete, A.; Didan, K.; Miura, T.; Rodriguez, E.P.; Gao, X.; Ferreira, L.G. Overview of the radiometric and biophysical performance of the MODIS vegetation indices. *Remote Sens. Environ.* **2002**, *83*, 195–213. [CrossRef]
8. Huete, A.; Justice, C.; Liu, H. Development of vegetation and soil indices for MODIS-EOS. *Remote Sens. Environ.* **1994**, *49*, 224–234. [CrossRef]
9. Ponce Campos, G.E.; Moran, M.S.; Huete, A.; Zhang, Y.; Bresloff, C.; Huxman, T.E.; Eamus, D.; Bosch, D.D.; Buda, A.R.; Gunter, S.A.; *et al*. Ecosystem resilience despite large-scale altered hydroclimatic conditions. *Nature* **2013**, *494*, 349–352. [CrossRef] [PubMed]
10. Xiao, X.; Hollinger, D.; Aber, J.; Goltz, M.; Davidson, E.A.; Zhang, Q.; Moore, B. Satellite-based modeling of gross primary production in an evergreen needleleaf forest. *Remote Sens. Environ.* **2004**, *89*, 519–534. [CrossRef]
11. Nagler, P.; Scott, R.; Westenburg, C.; Cleverly, J.; Glenn, E.; Huete, A. Evapotranspiration on western U.S. rivers estimated using the Enhanced Vegetation Index from MODIS and data from eddy covariance and Bowen ratio flux towers. *Remote Sens. Environ.* **2005**, *97*, 337–351. [CrossRef]
12. Shabanov, N.; Vargas, M.; Miura, T.; Sei, A.; Danial, A. Evaluation of the performance of Suomi NPP VIIRS top of canopy vegetation indices over AERONET sites. *Remote Sens. Environ.* **2015**, *162*, 29–44. [CrossRef]
13. Miura, T.; Turner, J.P.; Huete, A.R. Spectral Compatibility of the NDVI Across VIIRS, MODIS, and AVHRR: An Analysis of Atmospheric Effects Using EO-1 Hyperion. *IEEE Trans. Geosci. Remote Sens.* **2013**, *51*, 1349–1359. [CrossRef]
14. Kim, Y.; Huete, A.R.; Miura, T.; Jiang, Z. Spectral compatibility of vegetation indices across sensors: Band decomposition analysis with Hyperion data. *J. Appl. Remote Sens.* **2010**, *4*, 43520. [CrossRef]
15. Miura, T.; Yoshioka, H. Hyperspectral data in long-term, cross-sensor continuity studies. In *Hyperspectral Remote Sensing of Vegetation*; Thenkabail, P.S., Huete, A.R., Eds.; CRC Press: Boca Raton, FL, USA, 2011; pp. 607–627.
16. Vargas, M.; Miura, T.; Shabanov, N.; Kato, A. An initial assessment of Suomi NPP VIIRS vegetation index EDR. *J. Geophys. Res. Atmos.* **2013**, *118*, 12301–12316. [CrossRef]

17. Obata, K.; Miura, T.; Yoshioka, H.; Huete, A.R. Derivation of a MODIS-compatible enhanced vegetation index from visible infrared imaging radiometer suite spectral reflectances using vegetation isoline equations. *J. Appl. Remote Sens.* **2013**, *7*, 073467. [CrossRef]
18. Steven, M.D.; Malthus, T.J.; Baret, F.; Xu, H.; Chopping, M.J. Intercalibration of vegetation indices from different sensor systems. *Remote Sens. Environ.* **2003**, *88*, 412–422. [CrossRef]
19. Trishchenko, A.P.; Cihlar, J.; Li, Z. Effects of spectral response function on surface reflectance and NDVI measured with moderate resolution satellite sensors. *Remote Sens. Environ.* **2002**, *81*, 1–18. [CrossRef]
20. Trishchenko, A.P. Effects of spectral response function on surface reflectance and NDVI measured with moderate resolution satellite sensors: Extension to AVHRR NOAA-17, 18 and METOP-A. *Remote Sens. Environ.* **2009**, *113*, 335–341. [CrossRef]
21. Van Leeuwen, W.J.D.; Orr, B.J.; Marsh, S.E.; Herrmann, S.M. Multi-sensor NDVI data continuity: Uncertainties and implications for vegetation monitoring applications. *Remote Sens. Environ.* **2006**, *100*, 67–81. [CrossRef]
22. D'Odorico, P.; Gonsamo, A.; Damm, A.; Schaepman, M.E. Experimental Evaluation of Sentinel-2 Spectral Response Functions for NDVI Time-Series Continuity. *IEEE Trans. Geosci. Remote Sens.* **2013**, *51*, 1336–1348. [CrossRef]
23. Gonsamo, A.; Chen, J.M. Spectral Response Function Compatibility Among 21 Satellite Sensors for Vegetation Monitoring. *IEEE Trans. Geosci. Remote Sens.* **2013**, *51*, 1319–1335. [CrossRef]
24. Gitelson, A.A.; Kaufman, Y.J. MODIS NDVI Optimization To Fit the AVHRR Data Series-spectral Considerations. *Remote Sens. Environ.* **1998**, *66*, 343–350. [CrossRef]
25. Gao, B.-C. A practical method for simulating AVHRR-consistent NDVI data series using narrow MODIS channels in the 0.5–1.0 μm spectral range. *IEEE Trans. Geosci. Remote Sens.* **2000**, *38*, 1969–1975.
26. Gunther, K.P.; Maier, S.W. AVHRR compatible vegetation index derived from MERIS data. *Int. J. Remote Sens.* **2007**, *28*, 693–708. [CrossRef]
27. Yoshioka, H.; Miura, T.; Huete, A.R. An isoline-based translation technique of spectral vegetation index using EO-1 Hyperion data. *IEEE Trans. Geosci. Remote Sens.* **2003**, *41*, 1363–1372. [CrossRef]
28. Yoshioka, H.; Miura, T.; Obata, K. Derivation of Relationships between Spectral Vegetation Indices from Multiple Sensors Based on Vegetation Isolines. *Remote Sens.* **2012**, *4*, 583–597. [CrossRef]
29. Yoshioka, H. Vegetation isoline equations for an atmosphere-canopy-soil system. *IEEE Trans. Geosci. Remote Sens.* **2004**, *42*, 166–175. [CrossRef]
30. NASA Goddard Space Flight Center. NASA NPP VIIRS LAND PEATE QA. Available online: http://landweb.nascom.nasa.gov/cgi-bin/NPP_QA/NPPpage.cgi?fileName=dataOrder&subdir=forPage (accessed on 25 December 2015).
31. Justice, C.O.; Román, M.O.; Csiszar, I.; Vermote, E.F.; Wolfe, R.E.; Hook, S.J.; Friedl, M.; Wang, Z.; Schaaf, C.B.; Miura, T.; *et al*. Land and cryosphere products from Suomi NPP VIIRS: Overview and status. *J. Geophys. Res. Atmos.* **2013**, *118*, 9753–9765. [CrossRef] [PubMed]
32. Solano, R.; Didan, K.; Jacobson, A.; Huete, A. *MODIS Vegetation Index User's Guide*; Terrestrial Biophysics and Remote Sensing Lab, the University of Arizona: Tucson, AZ, USA, 2010; Volume 2010.
33. Friedl, M.A.; Sulla-Menashe, D.; Tan, B.; Schneider, A.; Ramankutty, N.; Sibley, A.; Huang, X. MODIS Collection 5 global land cover: Algorithm refinements and characterization of new datasets. *Remote Sens. Environ.* **2010**, *114*, 168–182. [CrossRef]
34. Loveland, T.R.; Belward, A.S. The IGBP-DIS global 1 km land cover data set, DISCover: First results. *Int. J. Remote Sens.* **1997**, *18*, 3289–3295. [CrossRef]
35. Vermote, E.; Justice, C.; Csiszar, I. Early evaluation of the VIIRS calibration, cloud mask and surface reflectance Earth data records. *Remote Sens. Environ.* **2014**, *148*, 134–145. [CrossRef]
36. Jackson, J.M.; Liu, H.; Laszlo, I.; Kondragunta, S.; Remer, L.A.; Huang, J.; Huang, H.-C. Suomi-NPP VIIRS aerosol algorithms and data products. *J. Geophys. Res. Atmos.* **2013**, *118*, 12673–12689. [CrossRef]
37. Liu, H.; Remer, L.A.; Huang, J.; Huang, H.-C.; Kondragunta, S.; Laszlo, I.; Oo, M.; Jackson, J.M. Preliminary evaluation of S-NPP VIIRS aerosol optical thickness. *J. Geophys. Res. Atmos.* **2014**, *119*, 3942–3962. [CrossRef]
38. Levy, R.C.; Remer, L.A.; Kleidman, R.G.; Mattoo, S.; Ichoku, C.; Kahn, R.; Eck, T.F. Global evaluation of the Collection 5 MODIS dark-target aerosol products over land. *Atmos. Chem. Phys.* **2010**, *10*, 10399–10420. [CrossRef]

39. Kopp, T.J.; Thomas, W.; Heidinger, A.K.; Botambekov, D.; Frey, R.A.; Hutchison, K.D.; Iisager, B.D.; Brueske, K.; Reed, B. The VIIRS Cloud Mask: Progress in the first year of S-NPP toward a common cloud detection scheme. *J. Geophys. Res. Atmos.* **2014**, *119*, 2441–2456. [CrossRef]
40. Jiang, Z.; Huete, A.R.; Didan, K.; Miura, T. Development of a two-band enhanced vegetation index without a blue band. *Remote Sens. Environ.* **2008**, *112*, 3833–3845. [CrossRef]